Mechanism of Olefin Asymmetric Hydrogenation Catalyzed by Iridium Phosphino-Oxazoline: A Pair Natural Orbital Coupled Cluster Study

Manuel Sparta,[†] Christoph Riplinger,[‡] and Frank Neese*,[†]

[†]Max-Planck-Institut für Chemische Energiekonversion, Stiftstr. 34-36, D-45470 Mülheim an der Ruhr, Germany
[‡]Department of Mechanical and Aerospace Engineering, Princeton University, Princeton, New Jersey 08544, United States

S *Supporting Information*

ABSTRACT: Since the development of chiral phosphino-oxazoline iridium catalysts, which hydrogenate unfunctionalized alkenes enantioselectively, the asymmetric hydrogenation of prochiral olefins has become important in the production of chiral compounds. For the last 10 years, details of the mechanism, including formal oxidation state assignment of the metal center and the nature of intermediates and transition states have been debated. Various contributions have been given from a theoretical point of view, but due to the size of the structures, these have been forced to rely on density functional theory (DFT) methods. In our investigation of the

catalytic cycle, we employ both DFT and a correlated *ab initio* method, namely, the newly implemented domain-based local pair natural orbital coupled-cluster theory with single and double excitations and the inclusion of perturbative triples correction (DLPNO-CCSD(T)). Our results show that the most likely active paths involve the formation of an intermediate Ir^V species. Furthermore, we have been able to predict the absolute configuration of the major products, and where comparison to experiment is possible, the results of our calculations agree with the enantiomeric excess obtained from hydrogenating five prochiral substrates. This work also shows that it is now possible to study catalytic reactions with untruncated models (having up to 88 atoms) at the CCSD(T) level of theory.
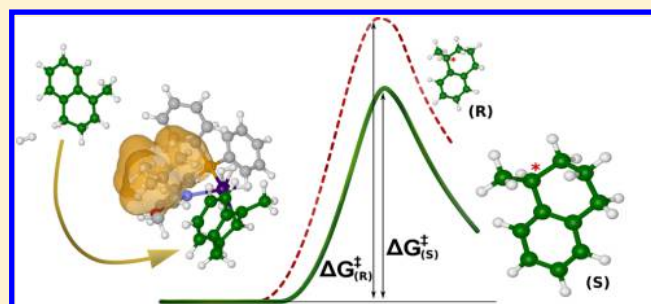
1. INTRODUCTION

The ability to systematically produce a specific enantiomer is of paramount importance in chemical synthesis. In the development of synthetic drugs, for example, frequently only the enantiomer with the proper absolute configuration shows pharmacological activity. This is due to the fact that most receptors that control biological functions are inherently asymmetric. Among the available methods to obtain chiral compounds starting from prochiral precursors, enantioselective hydrogenation is one of the most powerful.[1] The first catalysts capable of promoting the asymmetric hydrogenation of a double bond were rhodium[2] or ruthenium[3] diphosphine complexes. However, the applicability of these catalysts is limited to olefinic substrates functionalized with a polar group, enabling bidentate coordination of the substrate to the metal center.[4] To overcome this limitation, in 1998 Pfaltz and co-workers, inspired by the work of Crabtree,[5] successfully used a chiral phosphino-oxazoline (PHOX, see Chart 1) iridium complex to promote the enantioselective hydrogenation of unfunctionalized alkenes.[6−8] Since the introduction of PHOX, a variety of chelating ligands have been developed according to the general recipe that couples a heterocycle containing an sp²-hybridized nitrogen atom with a trisubstituted phosphorus (or N-heterocyclic carbene).[9]

Chart 1. PHOX Ligand (L)
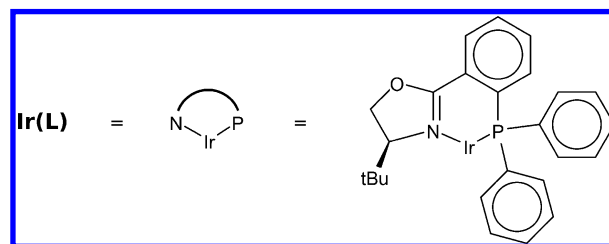
The catalytic cycle promoted by the Ir-PHOX complex has been at the center of debate, especially with regard to the oxidation state of the metal center and the nature of transition states and intermediates. Scheme 1 illustrates the proposed mechanisms. Andersson and co-workers[10] suggested a catalytic cycle involving both the iridium(III) and iridium(V) oxidation states (see Ir^{III}/Ir^V in Scheme 1). Starting from the hydride complexes **A**, namely $[(L)Ir(H)_2(solv)_2]^+$, (where solv symbolizes a solvent molecule) a simple solvent-olefin exchange reaction generates the adduct $[(L)Ir(H)_2(olefin)(solv)]^+$ (**B**). Further solvent exchange by molecular hydrogen leads to the

Scheme 1. Proposed Catalytic Mechanisms[a]
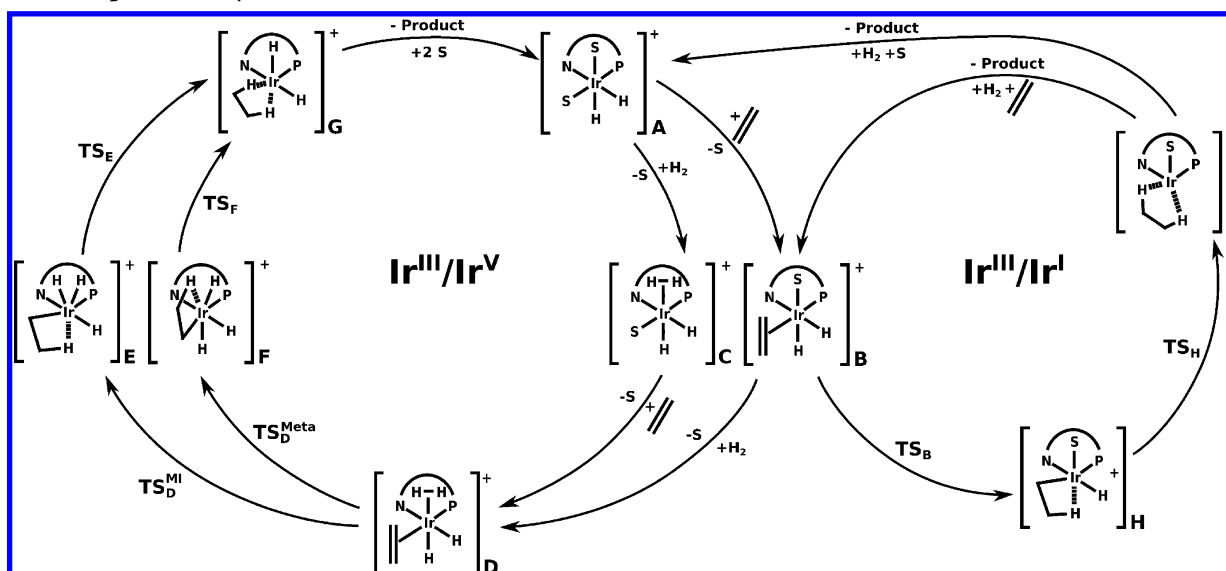
[a]In the depicted examples, the substrate coordinates *trans* to the P terminus and the hydrides are *trans* to the N terminus and below the N−Ir−P plane. For each of the intermediates and transition states different arrangements of the ligands are considered (e.g., substrate *trans* to the N terminus). S represents a solvent molecule.

formation of the $[(L)Ir(H)_2(H_2)(olefin)]^+$ moiety (**D**), the species identified as the resting state.[10] The formal oxidation state of iridium in each of these moieties is (III). Once **D** is generated, the formation of the C−H bond occurs with either migratory insertion into the metal hydride bond, concomitant with the breaking of the H−H bond (via TS_D^{MI}), or via a metathesis reaction with the bound H_2.[11,12] In both cases, the formal oxidation state of iridium in intermediates **E** and **F** is (V). These intermediates undergo reductive elimination (formation of the second C−H bond), restoring the original oxidation state (III) of the metal. Subsequent dissociation of the weakly bound alkane and coordination of two solvent molecules restore the structure **A**. Alternatively, a mechanism involving the alternation of iridium(III) and iridium(I) species, reminiscent of the cycle for the rhodium diphosphine-catalyzed hydrogenation of olefins,[13] has been postulated.[14] According to the Ir^{III}/Ir^I mechanism, the migratory insertion of the olefin into the metal hydride bond (formation of the first C−H bond) occurs in complex **B**. The product of this step is the alkyl species (**H**). This can undergo reductive elimination, leading to the alkane product being loosely coordinated to the metal in its (I) formal oxidation state (species **I**). Solvent complexation and H_2 oxidative addition then restore $[(L)Ir(H)_2(solv)_2]^+$, completing the catalytic cycle. Through detailed mass spectrometric studies, Dietiker and Chen concluded that the gas-phase reaction occurs via a Ir^{III}/Ir^I mechanism.[14]

Recently, two independent theoretical studies from Andersson and co-workers[15] and Hopmann and Bayer[16] investigated the possible catalytic mechanisms, and each concluded that the Ir^{III}/Ir^V cycle is energetically favored. These works provide a solid foundation for understanding the reaction mechanism. However, both studies exclusively relied on density functional theory (DFT) in terms of the B3LYP functional,[17−21] and the effect of the solvent environment was accounted for as a correction in a single point (SP) calculation fashion by the use of an implicit solvation model. Additionally, empirical van-der-Waals corrections[22] were included only in the final SP calculations (ref 16) or were neglected altogether (ref 15).

Subsequently, pyranoside phosphite oxazoline ligands were investigated in a combined experimental and computational study by Mazuela et al.;[23] the authors demonstrated that free energy calculations at DFT-D level of theory allow a computational determination of the observed selectivities with high accuracy.[23]

Since there are several subtle differences between the reaction mechanisms, and significant errors for DFT reaction barriers in transition metal catalyzed reactions can occur,[24,25] we believe that it is worthwhile to investigate the reaction mechanism using high-level wave function based *ab initio* methods. Among the possible *ab initio* methods, the coupled-cluster method (CC) stands out as being particularly accurate and robust.[26] However, until recently, the computational expense of CC studies was too high for being applied to realistic models of catalytic systems. This has changed through the advent of local correlation theories.[27−31] In this study, we use the domain-based local pair natural orbital coupled-cluster methodology with single and double excitations and perturbative triples correction (DLPNO-CCSD(T)), developed in our group.[32,33] This method combines a number of desirable features such as efficiency, robustness, and accuracy as well as black-box functionality. This is the first study to employ the DLPNO-CCSD(T) method. However, its predecessor, LPNO-CCSD (local pair natural orbital coupled-cluster methodology with single and double excitations),[34,35] has been employed previously yielding high quality results for investigating the mechanism of prochiral enamide hydrogenation[36] and weakly bound molecular systems.[37] We note that the computational expense associated with a DLPNO-CCSD(T) calculation exceeds the cost of a hybrid DFT calculation (without using approximations) by only 2−4 times. Hence, it is entirely feasible to employ DLPNO-CCSD(T) as a routine tool in computational quantum chemistry.

In this article, we present our work on the asymmetric hydrogenation promoted by Ir-PHOX. Using ethylene as a prototypical substrate, we have investigated the complete catalytic cycle, characterizing all intermediates and transition

states for a variety of possible mechanisms to identify the most likely active pathways. Subsequently, we refined our conclusions by studying five different prochiral substrates, for each of which experimental data is available for similar catalysts (*vide infra*). This allows us to assess the ability of the applied methodology to predict the absolute configuration of the major product. Concerning the computational approach, we employed DFT together with empirical dispersion correction and inclusion of solvent effects in the determination of stationary structures. Finally, the energies of all species were calculated with the DLPNO−CCSD(T) method, and the results were compared to DFT energies.

2. COMPUTATIONAL DETAILS

2.1. Geometry Optimization and Thermochemical Corrections. Geometry optimizations were carried out using DFT with the BLYP functional[17−21] in combination with the resolution of identity (RI) approximation.[38] All calculations employed the scalar relativistic, all-electron ZORA approach in conjunction with the model potential concept of van Wüllen.[39] Def2-SVP and def2-TZVP basis sets[40−42] were used for lighter atoms and for chlorine and phosphorus, respectively, and the segmented all-electron relativistically contracted (SARC) TZVP basis was used for iridium.[43] Considering the flexibility of the systems studied, the conformational isomers of the complexes were extensively investigated to locate the lowest energy conformers.

Dispersion contributions were included in both energy and gradient calculations via the empirical correction, as implemented by Grimme.[22] Solvation effects were accounted for using the Conductor-like Screening Model (COSMO);[44] the solvent is treated as a continuum with a permittivity corresponding to that of dichloromethane ($\varepsilon = 9.08$).

The nature of all stationary structures was characterized by frequency calculations (two-sided numerical differentiation). Thermochemical corrections to the energies were computed from the unscaled harmonic frequency for a temperature of 298.15 K.[45] To correct for the breakdown of the harmonic oscillator approximation for low frequencies, entropic contributions to the free energies were computed using the Quasi-RRHO approach of Grimme.[46] This approach was found to be significantly more robust than to neglect the contribution of small frequencies.

2.2. Single Point Energy Calculations. Final electronic energies were obtained by means of single point calculations (SP) using both *ab initio* DLPNO-CCSD(T)[32,33] and DFT, employing a variety of functionals including: B3LYP,[17−21] TPSSh,[17,18,47−49] both used in combination with empirical dispersion corrections[22] to form the corresponding DFT-D estimates and M06-L as well as its hybrid counterpart M06-2X.[50,51] The def2-TZVP basis set[40−43] and the RIJCOSX approximation[52,53] were used in all single point calculations. All calculations were performed using the ORCA program package (versions 2.9 and 3.0).[54]

2.3. Gibbs Free Energy in Solution. Energies discussed in the following sections are all Gibbs free energies at 298.15 K. For each level of theory, these were calculated by combining the electronic energy computed by means of SP energy calculations (e.g., $E_{el/gas}^{DLPNO-CCSD(T)/SP}$) with the thermochemical corrections evaluated at the geometry optimization level of theory ($(G - E_{el})^{BLYP/opt}$). The values were corrected to account for the change in standard states in going from the gas phase to the condensed phase (1 mol L^{-1} and 298.15 K)

$\Delta G^{0\rightarrow *}$ = 1.89 kcal/mol. For dichloromethane and THF a standard state of 15.6 and 12.3 mol L^{-1} at 298.15 K was used, respectively. Consequently, their respective $\Delta G^{0\rightarrow *}$ values were computed to be equal to 3.51 and 3.38 kcal/mol.

For the DFT calculations, solvation effects were accounted for using COSMO in the SP calculations, whereas for the *ab initio* data a solvation correction was used, computed as the energy difference between the SP energy calculated at B3LYP level of theory with and without the COSMO correction. Specifically, the Gibbs free energy for each moiety is computed as $G = E_{el/gas}^{DLPNO-CCSD(T)/SP} + (G - E_{el})^{BLYP/opt} + \Delta G^{0\rightarrow *} + (E_{el/solv}^{B3LYP} - E_{el/gas}^{B3LYP})$ for the *ab initio* method and as $G = E_{el/solv}^{DFT/SP} + (G - E_{el})^{BLYP/opt} + \Delta G^{0\rightarrow *}$ for the various DFT functionals.

3. RESULTS

3.1. Relative Stability of the $[(L)Ir(H)_2(solv)_2]^+$ Complexes. In 2004, Mazet et al. investigated hydrido iridium complexes by means of experimental and computational techniques in an attempt to shed light on the elusive intermediates generated during the hydrogenation process.[55] The reaction could not be followed by NMR if deuterated dichloromethane was used as a solvent. In the presence of tetrahydrofuran (THF, a more strongly coordinating solvent), the selective formation of two complexes of formula $[(L)Ir(H)_2(solv)_2]^+$ was observed. These complexes were identified with the two hydride ligands located *cis* to each other and *cis* to the phosphorus atom (**A1** and **A3** in Chart 2). DFT calculations using CH_2Cl_2 as solvent showed the relative energies of the various isomers of $[(L)Ir(H)_2(solv)_2]^+$ to be in agreement with the experimental data.[10,15,55]

Chart 2. $[(L)Ir(H)_2(solv)_2]^+$ **Isomers Considered in This Work**
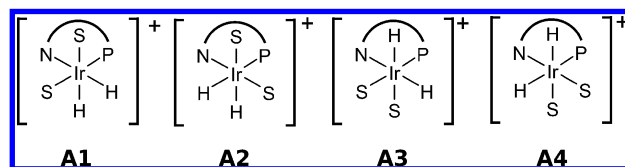
We investigated the relative stabilities of the isomers presented in Chart 2 for both THF and dichloromethane. In both cases, **A3** was found to be most stable, followed by **A1** (see Table 1). This is in agreement with previously reported computational (CH_2Cl_2) and experimental (THF) data. It should be mentioned that the large energy difference between **A3** and **A1** (7.4 kcal/mol) does not conflict with their detection at room temperature, since it was postulated that the reaction leading to the formation of the two hydrides is not under thermodynamic control.[55]

Additionally, we computed the free energy for solvent substitution by dihydrogen and found that in the presence of THF, the substitution of the coordinated solvent with H_2 is endergonic (e.g., for **A3** $\Delta G = 3.8$ kcal/mol). Conversely, as a consequence of the more weakly coordinating strength of CH_2Cl_2, H_2 substitution is more facile (e.g., for **A3** $\Delta G = 0.9$ kcal/mol). These data are in agreement with the selective formation of two hydride complexes of formula $[(L)Ir(H)_2(THF)_2]^+$ and also explain the formation of a complex mixture of hydrido complexes which could not be analyzed if CD_2Cl_2 was used, as reported by Mazet et al.[55]

3.2. Catalytic Cycle with Ethylene as Substrate. In order to gain insight into the details of the catalytic process, we

Table 1. Relative Stabilities of the $[(L)Ir(H)_2(solv)_2]^+$ Isomers[a]

	CH$_2$Cl$_2$			THF		
	B3LYP-D	TPSSh-D	DLPNO-CCSD(T)	B3LYP-D	TPSSh-D	DLPNO-CCSD(T)
A1	3.2	3.4	3.8	7.4	7.8	7.7
A2	16.0	15.4	15.9	16.6	16.2	16.8
A3	0.0	0.0	0.0	0.0	0.0	0.0
A4	10.7	9.9	11.7	10.1	9.9	11.5

[a]Free energies are given in kcal/mol and are relative to the energy of **A3** (see Chart 2).

first investigated the Ir^{III}/Ir^V and Ir^{III}/Ir^I families of mechanisms, presented in Scheme 1, using ethylene as a prototypical substrate. For each intermediate and transition state, a variety of isomers were identified (*vide infra*). In addition, each pathway was characterized by calculating its activation energy to determine those that are most likely to be active.

3.2.1. Ir^{III}/Ir^V Mechanisms. During the investigation of the possible isomers of the **B** complexes (see Chart 3), we

Chart 3. B (X = CH$_2$Cl$_2$) and D (X = H$_2$) Isomers Considered in This Work
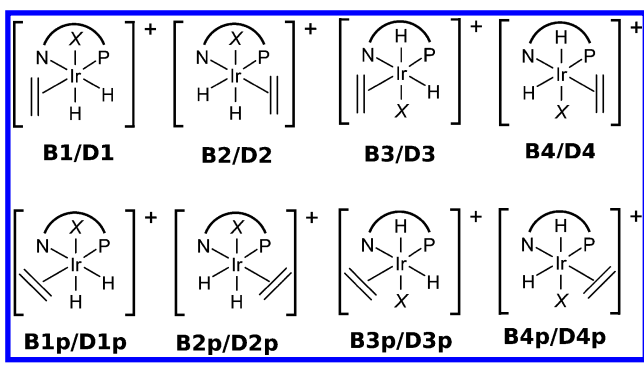
considered all structures that could be generated by simple substitution of a solvent molecule in the four isomers of **A**. In order to limit computational effort, we restricted the search to structures where ethylene was *trans* to either the N or P terminus of the ligand L, yielding a total of eight isomers. Further simple substitution of the remaining solvent molecule by molecular hydrogen generates the eight **D** structures (as in Chart 3). Moreover, Chart 3 illustrates the conventions adopted in this work to label the different species (see ref 56 for additional details).

Considering the different arrangement of the substrate in the **D** species, it is clear that when the double bond lies in the plane defined by the N−Ir−P, (**D[1−4]p**), the substrate has direct access to migratory insertion into the M−H *trans* to either N or P. On the contrary, if the double bond lies orthogonal to the N−Ir−P plane, both the migratory insertion and metathesis processes are viable. This leads to a total of twelve possible ways of forming the first C−H bond (four **TS$_D^{Meta}$** and eight **TS$_D^{MI}$**) and, consequently, twelve possible intermediates (**E** and **F**).

For some of these intermediates, a local minimum in the potential energy surface (PES) could not be determined. Hence, the total number of **E** and **F** intermediates sums to eight. The subsequent formation of the second C−H bond occurs via a reductive elimination step that generates a weakly bound alkane (structures **G**).

In summary, starting with the four isomers presented in Chart 2, and considering the eight isomers of $[(L)Ir(H)_2(H_2)\text{-}(ethylene)]^+$ (see Chart 3), we were able to identify nine variations of the Ir^{III}/Ir^V mechanism capable of completing the catalytic cycle. The data are presented in Table 2. Figure 1 shows the energetic profiles for the nine mechanisms given with respect to the cumulative free energy of complex A3, H$_2$, and ethylene.

Analysis of Table 2 and Figure 1 confirms that the structures of type **D** are the resting state for the catalytic process occurring in dichloromethane. This is in agreement with the kinetic data,

Table 2. Ir^{III}/Ir^V Mechanism, Paths, and Free Energies Computed at the DLPNO-CCSD(T) level of Theory[a]

path	MI-1		MI-2		MI-3	
	A1	3.8	A2	15.9	A3	0.0
	B1	−4.4	B2	−0.8	B3	−6.7
	D1	−12.0	D2	−6.7	D3	−10.4
	TS$_D^{MI}$1	**−3.0**	**TS$_D^{MI}$2**	**5.6**	**TS$_D^{MI}$3**	**−0.2**
	E1	−7.4	F2	−2.5	E3	−2.6
	TS$_E$1	−7.6	TS$_E$2	−1.8	TS$_E$3	−0.4
	G1	−16.9	G2	−1.8	G3	−13.2
ΔG‡	**9.0**		**17.6**		**11.8**	
path	MI-4p[b]		MI-4p'[b]		MI-4	
	A4	11.7	A4	11.7	A4	11.7
	B4p	−6.7	B4p	−6.7	B4	−4.8
	D4p	−7.4	D4p	−7.4	D4	−5.8
	TS$_D^{MI}$4	−2.0	TS$_D^{MI}$4p	−2.0	**TS$_D^{MI}$4**	**4.1**
	E4p	−4.6	E4p	−4.6	E4	−9.5
	TS$_E$4p	**11.2**	**TS$_E$4p'**	**5.3**	TS$_E$4	0.7
	G5	7.8	G5'	6.8	G2	−1.8
ΔG‡[c]	**23.2**		**17.3**		**16.1**	
path	Meta-1		Meta-3		Meta-4	
	A1	3.8	A3	0.0	A4	11.7
	B1	−4.4	B3	−6.7	B4	−4.8
	D1	−12.0	D3	−10.4	D4	−5.8
	TS$_D^{Meta}$1	**−1.1**	**TS$_D^{Meta}$3**	**−0.6**	**TS$_D^{Meta}$4**	**10.7**
	F1	−1.3	F3	−1.0	F4	12.2
	TS$_F$1	−2.8	**TS$_F$3**	**−0.4**	**TS$_F$4**	**15.9**
	G1	−16.9	G3	−13.2	G4	−0.4
ΔG‡[c]	**10.9**		**11.6**		**27.9**	

[a]Energies are given in kcal/mol and are relative to the cumulative energy of A3, H$_2$, and ethylene. [b]In **D4p** the double bond lies on the P−Ir−N plane, *trans* to the N terminus of the ligand. After the formation of the C−H bond (**E4p**), two paths for the final reductive elimination are possible involving the hydrogens above or below the P−Ir−N plane (via **TS$_E$4p** or **TS$_E$4p'**). [c]Activation energies are given in kcal/mol, computed as the energy difference between the most stable **D** isomer (**D1**) and the rate determining transition state for each path (highlighted with bold font).
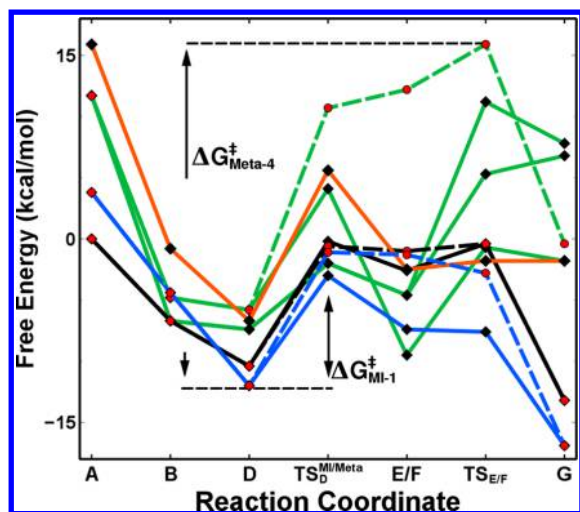
Figure 1. Free energy for the catalytic cycle of ethylene hydrogenation following the Ir^{III}/Ir^V mechanisms. Black diamonds and solid lines: mechanisms involving migratory insertion into a M–H bond; Red dots and dashed lines: metathesis reaction with the bound H_2. Energies are given in kcal/mol relative to the $G(A3 + H_2 + ethylene)$. Line color code: paths originating from complex **A1** (blue); **A2** (orange); **A3** (black); **A4** (green).

which show no dependency on the alkene concentration when extremely weakly coordinating counterions are used.[57]

Moreover, we note that except for structure **D4p**, none of the complexes in which the ethylene double bond is coplanar with N–Ir–P are found to be an intermediate in an active path. It is interesting to observe that for intermediate **D**, **D1** is computed to be more stable than **D3**, inverting the trend observed for the parent **A** (**A3** was found to be lower in energy than **A1**). Additionally, the energy span of the **D** complexes is significantly smaller than its counterpart in the **A** complexes (the energy difference between **A3** and **A2** is equal to 15 kcal/mol, whereas the **D1** and **D4** are separated by ca. 6 kcal/mol).

To compute the activation energy, the rate determining states for each of the possible paths must be identified (for a recent discussion regarding the computation of activation energies in catalytic cycles, we refer to ref 58). Given the shape of the potential energy surfaces represented in Figure 1, the TS for the formation of the first C–H bond is rate determining for the paths MI-1, MI-2, MI-3, MI-4, and Meta-1, whereas the formation of the second C–H bond is rate limiting for the remaining pathways. Additionally, the rate determining intermediate has to be identified considering that competing mechanisms are taking place and assuming rapid interconversion of the **D** moieties. We note that the activation energy to convert **D1** into **D3** is significantly smaller than the activation energy for the C–H bond formations, supporting the assumption that the **D** species are rapidly interconverting. On the other hand, **D2** and **D4** cannot be directly obtained from **D1** nor **D3**, and it was assumed that their parental complexes could be obtained earlier in the reaction path (at intermediate **B** or **C**). This was not further investigated as paths involving **D2** and **D4** were deemed inactive (*vide infra*). Invoking an extension of the Curtin–Hammett Principle,[59] the most stable of the **D** species must be used for computing the activation energy for all paths. In Figure 1, a graphic representation of the method by which the activation energy is computed is shown for the paths MI-1 and Meta-4 (Table 2).

Our calculations suggest that the paths passing through **D2** and **D4** are inactive during catalysis since their rate limiting step is predicted to be considerably higher than the paths passing through **D1** and **D3** (see, for instance, $TS_D^{MI}4$ at 4.1 kcal/mol vs $TS_D^{Meta}3$ at −0.4 kcal/mol and the corresponding $\Delta G_{MI-4}^\ddagger = 16.1$ and $\Delta G_{Meta-3}^\ddagger = 11.6$). A different situation is observed for the paths involving **D4p**. In that case, the first C–H formation is facile ($TS_D^{MI}4p$), but the formation of the second C–H bond is associated with high energy transition states (two paths are possible, involving either the hydrogens above or below the P–Ir–N plane), leading to an activation energy of 23.2 and 17.3 kcal/mol for MI-4p and MI-4p′, respectively.

Concerning the comparison between the DFT and *ab initio* results, we observe that all of the methods adopted in this study provide the same overall picture regarding the main PES features. DLPNO−-CCSD(T) and B3LYP-D show good agreement and predict the migratory insertion to be the preferred mechanism, whereas at TPSSh-D level of theory, both activation energies for the metathesis process Meta-1 and Meta-3 (via $TS_D^{Meta}1$ and $TS_D^{Meta}3$, respectively) are lower than their counterparts involving migratory insertions MI-1 and MI-3 ($TS_D^{MI}1$ and $TS_D^{MI}3$); see Table 3. The question regarding

Table 3. Free Energy of Activation for the Possible Ir^{III}/Ir^V Paths as Function of the Computational Method[a]

	DLPNO-CCSD(T)	B3LYP-D	TPSSh-D
MI-1	9.0	9.9	9.0
MI-2	17.6	18.8	17.7
MI-3	11.8	12.8	12.1
MI-4p	23.2	23.0	21.0
MI-4p′	17.3	16.8	18.5
MI-4	16.1	16.3	15.1
Meta-1	10.9	10.7	8.8
Meta-3	11.6	12.1	10.6
Meta-4	27.9	27.3	24.7

[a]Energies are given in kcal/mol and computed as the energy difference between the most stable **D** isomer (**D1**) and the rate determining transition state for each path.

whether the catalyst promotes the metathesis process or migratory insertion has been addressed by Andersson and co-workers[15] and by Hopmann and Bayer.[16] In each case, the authors concluded (using B3LYP or B3LYP-D) that the migratory insertion is the preferred pathway. Mazuela et al. reached the same conclusions for a significantly different ligand.[23]

In conclusion, analysis of the possible Ir^{III}/Ir^V paths argues for active mechanisms where the substrate is initially coordinated *trans* to the P terminus of the PHOX ligand. In agreement with previous results, the migratory insertion mechanism is predicted to be favored over the metathesis process. However, a firm conclusion cannot be drawn at this stage since only the model substrate ethylene was used. Below, we will investigate the migratory insertion and metathesis process, for a set of realistic prochiral substrates, starting from the complexes **D1** and **D3** to determine the most likely pathway.

3.2.2. Ir^{III}/Ir^I Family of Mechanisms. According to the alternative Ir^{III}/Ir^I mechanism, the migratory insertion of the double bond into the metal hydride bond occurs in structure **B** (prior to the complexation of molecular hydrogen), leading to the **H** intermediates.

As for the previous mechanism, we exhausted all possibilities by investigating each of the structures included in Chart 3 as a possible starting point. Only in three cases did migratory insertion produce a stable intermediate, namely **H2**, **H2p**, and **H4p**, generated starting from **B2**, **B2p**, and **B4p**, respectively. Hence, the paths that follow the Ir^{III}/Ir^{I} mechanism involve the coordination of the substrate *trans* to the N terminus of the PHOX ligand.

Supporting Information (SI) Figure S1-A depicts the three possible paths that complete the catalytic cycle following the Ir^{III}/Ir^{I} mechanism, whereas SI Table S1 provides the energy of the stationary points. In contrast to the results obtained for the majority of the Ir^{III}/Ir^{V} mechanisms, the formation of the second C—H bond is predicted to be the rate determining transition state. To determine the activation energy for each path, one has to consider not only the height of the rate determining transition state, but also the energy of the stable intermediates on competing mechanisms. **D1** was determined to be the thermodynamic sink with an energy of −12.0 kcal/mol. The activation energies, calculated using **D1** as reference, are much larger than for several of the Ir^{III}/Ir^{V} paths. Even the one with the lowest activation energy ($MI^{III/I}$-4p: $\Delta G^{\ddagger} = 16.6$ kcal/mol) is unlikely to be active compared to the aforementioned Ir^{III}/Ir^{V} paths (see SI Figure S2,B). In conclusion, our data suggest that the high oxidation state routes are more feasible, as originally suggested by Brandt et al.,[10] in agreement with recent theoretical investigations.[15,16]

3.3. Hydrogenation of Prochiral Substrates. By comparative analysis of the catalytic paths for the Ir-PHOX catalyzed hydrogenation of ethylene, we determined that the paths most likely to be active are those through the **D1** and **D3** complexes. Furthermore, we identified that the first C—H bond formation is rate determining for these pathways.

Chart 4 shows the prochiral substrates investigated in this work. **Sub1** ((E)-1,2-diphenyl-1-propene) is representative of

Chart 4. Prochiral Substrates
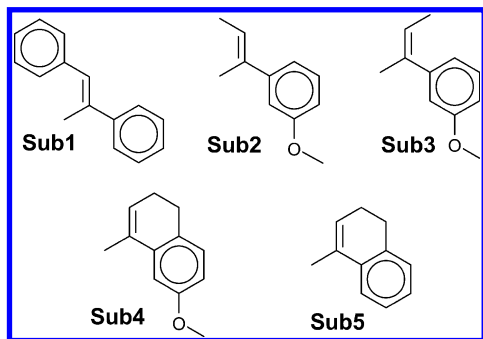
the class of olefins with two aryl groups in a *trans* arrangement. These are hydrogenated with high enantioselectivity by many different catalysts. It has been experimentally established that a PHOX ligand with (S) absolute configuration, as in the case of the one investigated in this work, produces a large enantiomeric excess (e.e.) in favor of the (R) product: Brandt et al. reported an enantiomeric excess in the range 89−91%,[10] whereas 97% has been obtained by substituting the $P(Ph)_2$ moiety on the PHOX ligand with $P(o\text{-Tol})_2$.[8] **Sub2** and **Sub3** ((E/Z)-2-(4-methoxyphenyl)-2-butene) give products of opposite absolute configuration: e.e. = 81% (R) and e.e. = 63% (S) are obtained to for the (E) and (Z) isomers, respectively.[8] For 1,2-dihydro-7-methoxy-4-methyl-naphthalene (**Sub4**), the observed enan-

tioselectivity is 72% in favor of the (S) product.[60] In the experiments involving **Sub2−4**, the $P(o\text{-Tol})_2$ modification of the PHOX ligand was employed, however the results are indicative of what could be obtained with PHOX. In fact, when a direct comparison between the $P(Ph)_2$- and $P(o\text{-Tol})_2$-based ligands exists, the latter is only found to increase the enantiomeric excess by a few percents.[6,8,61] The last substrate investigated in this work is 1,2-dihydro-4-methyl-naphthalene (**Sub5**). This, in spite of the structural similarity to **Sub4**, gives lower enantiomeric excess than its methoxy derivative.[15,62] In these studies, however, the chiral center was significantly different from the one in PHOX; therefore, the results cannot be generalized for the PHOX ligand.

A trisubstituted olefin can coordinate to each **D1** and **D3** in four different ways (I−IV), uniquely determined by the orientation of the C=CH subunit, as shown in Chart 5 for

Chart 5. Four Nonequivalent Coordination Modes of a Prochiral Substrate to a D1 Structure[a]
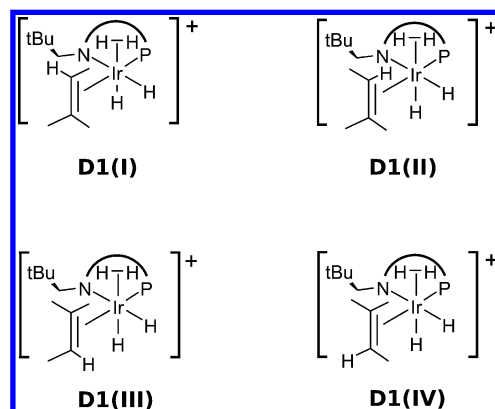
[a]The bulky substituent on the oxazoline ring is shown for reference.

D1. For each substrate, eight inequivalent isomers must be considered. As previously described in the case of ethylene, each of the **D**-type complexes can undergo migratory insertion (via a TS_D^{MI} transition state) or a metathesis process (via a TS_D^{Meta} transition state) for a total of 16 transition states. We observe that, whereas the orientation of the substrate (I−IV) in the **D** complexes determines the absolute configuration of the product, the enantioselectivity of the process is governed by the relative energy of the transition states and is independent of the energy of the intermediates (Curtin−Hammett Principle).[59]

In this case, the equilibrium between the **D** complexes (orientations I−IV) is achieved via two consecutive solvent−substrate exchanges (generation of a transient **C** complex). The computed energies show that, in general, this process is more facile than the formation of the C−H bond via TS_D^{MI} or TS_D^{Meta}, supporting the assumption that the **D** complexes are rapidly interconverting.

3.3.1. Migratory Insertion. In the study of realistic prochiral substrates, we have conservatively decided to calculate the relative stability of 8 possible intermediates and 16 transition states. The relative energies computed for **Sub1−5** are reported in SI Tables S2−S6, and the analysis of the data allows some general conclusions to be determined regarding the most likely paths. First, regardless of the mechanism for the C−H bond formation, the intermediates and transition states of type **D3** are found to be higher in energy than corresponding stationary points of type **D1**. Second, at the DLPNO-CCSD(T) level of

Table 4. Asymmetric Hydrogenation of Sub1[a]

Sub1[b]		B3LYP	B3LYP-D	TPSSh	TPSSh-D	M06-L	M06-2X	DLPNO-CCSD(T)
(I)	(R)	**8.9**	**8.9**	**8.3**	**8.2**	**8.5**	**7.4**	**7.2**
(II)	(S)	13.7	**11.2**	12.7	**10.6**	**11.3**	**10.2**	11.5
(III)	(R)	14.7	15.6	14.3	15.0	15.7	14.0	14.7
(IV)	(S)	**11.9**	**11.3**	**10.9**	**10.2**	**11.0**	**9.6**	**10.2**
$\Delta\Delta G^{\ddagger}_{(S)-(R)}$		3.0	2.3	2.6	2.0	2.5	2.2	3.0
e.e.[c] (R)		99	93	97	90	96	94	98

[a]Free energy of activation for the olefin migratory insertion as function of the relative orientation of the substrate and level of theory adopted. Energies are given in kcal/mol and are relative to the energy of the most stable **D** complex. [b]Explanation of the relative orientation of the substrate (I−IV) is given in Chart 5. For each orientation, the absolute configuration of the corresponding product is given. Bold fonts mark paths with significant activity (>1%) in the generation of the (R) and (S) products. [c]Computed using all four activation energies.

Table 5. Asymmetric Hydrogenation of Sub2 and Sub3[a]

Sub2[b]		B3LYP	B3LYP-D	TPSSh	TPSSh-D	M06-L	M06-2X	DLPNO-CCSD(T)
(I)	(R)	**11.1**	**10.6**	**10.2**	**9.6**	**10.6**	**10.0**	**9.5**
(II)	(S)	**13.2**	14.2	**12.4**	13.2	14.3	13.8	13.8
(III)	(R)	**13.5**	17.5	**12.9**	16.3	16.2	15.8	17.4
(IV)	(S)	**11.8**	**12.2**	**10.6**	**10.9**	**11.8**	**11.0**	**11.7**
$\Delta\Delta G^{\ddagger}_{(S)-(R)}$		0.7	1.6	0.4	1.3	1.2	1.0	2.2
e.e.[c] (R)		47	88	31	80	75	71	95
Sub3[b]		B3LYP	B3LYP-D	TPSSh	TPSSh-D	M06-L	M06-2X	DLPNO-CCSD(T)
(I)	(S)	**10.6**	**9.9**	**9.2**	**8.3**	**10.4**	**9.1**	**7.1**
(II)	(R)	15.3	**11.3**	13.6	**9.8**	**11.7**	**10.8**	**8.4**
(III)	(S)	15.6	**11.2**	13.6	**9.5**	**11.2**	**9.9**	**8.4**
(IV)	(R)	14.4	16.1	12.9	14.1	15.2	14.5	14.5
$\Delta\Delta G^{\ddagger}_{(R)-(S)}$		3.8	1.4	3.7	1.5	1.3	1.6	1.3
e.e.[c] (S)		>99	86	>99	83	89	91	83

[a]Free energy of activation for the olefin migratory insertion as function of the relative orientation of the substrate and level of theory adopted. Energies are given in kcal/mol and are relative to the energy of the most stable **D** complex. [b]Explanation of the relative orientation of the substrate (I−IV) is given in Chart 5. For each orientation, the absolute configuration of the corresponding product is given. Bold fonts mark paths with significant activity (>1%) in the generation of the (R) and (S) products. [c]Computed using all four activation energies.

theory, the migratory insertion pathways are preferred over the metathesis processes by 4−5 kcal/mol. We note that the same conclusions are obtained at DFT level of theory. Even TPSSh-D, which gave qualitatively different results in the ethylene case, predicts the migratory insertion mechanism to be preferred by 2−3 kcal/mol. These observations, based on both *ab initio* and DFT results on a set of five realistic prochiral substrates, are in agreement with the conclusions, obtained with DFT, by Andersson and co-workers[15] and by Hopmann and Bayer[16] for the PHOX ligand and by Mazuela et al.[23] for pyranoside phosphite−oxazoline ligand.

Based on these results, we expect that it is possible to predict the absolute configuration of the major product in the hydrogenation by focusing on the analysis of the transition states for the migratory insertion occurring in a **D1** type of complex, that is, comparing the relative energy of the transition states **TS**$_D^{MI}$**1(I−IV)**.

3.3.2. Sub1: (E)-1,2-diphenyl-1-propene. The relative energies for the stationary points (8 intermediates and 16 transition states) are summarized in SI Table S2. We note that the coordination (I) and (III) in Chart 5 leads to the (R) product, whereas (II) and (IV) would produce the (S) enantiomer. As expected, the most stable isomers of the **D** complexes are **D1(I)** and **D3(I)**. In these adducts, the substrate is oriented such that the olefinic H points in the direction of the *tert*-butyl group, and a phenyl group is stacked with the oxazoline ring as initially observed by Brandt et al.[10] Each of the other rotamers have either the methyl or a phenyl group

interacting with the bulky substituent and are found at higher energy.[16] Our data are in agreement with the results of Hopmann and Bayer[16] regarding the most stable intermediate, with the only difference being a larger energy span between the different isomers, probably due to the larger *tert*-butyl group investigated in this study.

Concerning the activation energy for the formation of the C−H bond, the lowest barrier is associated with the migratory insertion occurring in the **D1(I)** adduct (7.2 kcal/mol via **TS**$_D^{MI}$**1(I)**). In agreement with the experimental data, this would give the (R) product. The second lowest activation barrier is observed for the migratory insertion occurring in the **D1(IV)** adduct (10.2 kcal/mol, via **TS**$_D^{MI}$**1(IV)**). Such a process would yield to the product with (S) absolute configuration. An overview for the different pathways (**TS**$_D^{MI}$**1(I−IV)**) is reported in Table 4 as function of the method employed in this study. For the asymmetric hydrogenation of **Sub1**, all of the DFT functionals, as well as DLPNO-CCSD(T), converge to the same aforementioned description.

Finally, we note that the relative activation energy differences determine the enantiomeric excess. For cases where the activation energies are well separated (see B3LYP in Table 4), $(\Delta\Delta G^{\ddagger}_{(S)-(R)})$ can provide an accurate estimate of the e.e., whereas cases where more than two paths show significant activity (e.g., B3LYP-D) require all the terms to be accounted for.

For the case under analysis, DLPNO−CCSD(T) predicts a e.e. = 98% in favor of the (R) product; $\Delta\Delta G^{\ddagger}_{(S)-(R)}$ = 3.0 kcal/

mol. Considering that a 89−91% e.e. was determined for the catalyst under investigation[10] (which corresponds to 1.7−1.8 kcal/mol difference in barrier height), for this system, the 98% e.e. predicted with DLPNO−CCSD(T) is an overestimation of the experimental data whereas the DFT values are in fair agreement. Notably, our results are in agreement with the results in ref 16, where the B3LYP-D $\Delta\Delta G^{\ddagger}_{(S)-(R)}$ for **Sub1** was computed to be 2.2 kcal/mol.

3.3.3. Sub2 and Sub3: (E)-2-(4-methoxyphenyl)-2-butene and (Z)-2-(4-methoxyphenyl)-2-butene. The relative energies for the eight intermediates and the corresponding transition states for the migratory insertion and metathesis process are reported in SI Tables S3 and S4 for **Sub2** and **Sub3**, respectively.

For the rationalization of the enantioselectivity of the process, we focus on the activation energy for the migratory insertion in the **DI(I−IV)** structures, for which the results from different levels of theory are collected in Table 5. In contrast to the case of **Sub1**, inclusion of dispersion corrections is fundamental for achieving a theoretical prediction of the enantioselectivity in agreement with the experimental evidence.

Sub1 has two phenyl groups in a *trans* arrangement, meaning that all of the substrate orientations defined in Chart 5 are stabilized either by the phenyl-oxazoline or by the phenyl-*tert*-butyl interaction, hence the uncorrected functionals provide accurate results due to a fortuitous error cancellation. For **Sub2**, large contributions to the dispersion energy stabilize only specific conformations; the phenyl ring on the substrate can interact with either the oxazoline ring (**D1(I)** and **TS$_D^{MI}$1(I)**, see Figure 2,A) or the *tert*-butyl group (**D1(IV)** and **TS$_D^{MI}$1(IV)**, see Figure 2,B).
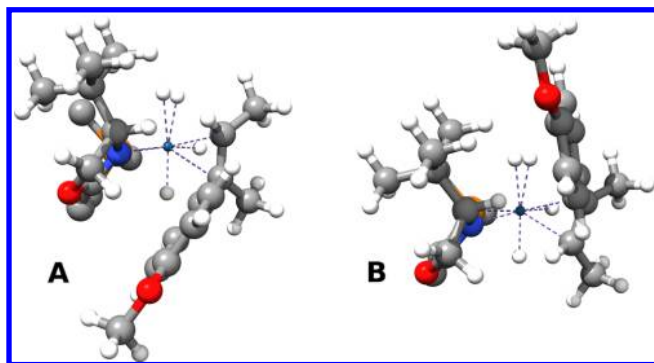
Figure 2. Interaction between the phenyl ring on the substrate with the oxazoline ring (A) or with the *tert*-butyl group (B). Phenyl rings on PHOX have been omitted for clarity.

Considering that the e.e. = 81% (R), obtained by employing the P(o-Tol)₂ modification of the PHOX ligand,[8] corresponds to a difference in the barrier height of ca 1.4 kcal/mol, it is clear that B3LYP and TPSSh are unable to describe the enantioselectivity of the process (low predicted e.e.). On the other hand, once the dispersion interactions are accounted for, the predicted enantiomeric excesses increase significantly and approach the result obtained with DLPNO-CCSD(T).

As observed for **Sub2**, the poor description of the dispersion interactions is responsible for the inaccurate prediction of the enantioselectivity of the process by B3LYP and TPSSh. In the case of **Sub3**, $\Delta\Delta G^{\ddagger}_{(R)-(S)}$ is overestimated (3.7−3.8 kcal/mol) compared to the *ab initio* and DFT-D results

The experimental e.e. = 63% (S) obtained with the P(o-Tol)₂ modification of the PHOX ligand[8] implies a barrier separation of ca 0.9 kcal/mol.

This is rationalized considering that the interactions described in Figure 2 occur when the substrate is coordinated in the (II) and (III) fashion. The importance of these interactions is evident in the fact that **D1(II)** is predicted to be the most stable of all intermediates (see SI Table S4). By neglecting these interactions, B3LYP and TPSSh incorrectly determine that the pathway passing via **TS$_D^{MI}$1(IV)** is the most likely to generate the (R) product, hence the overestimation of $\Delta\Delta G^{\ddagger}_{(R)-(S)}$. In contrast, DFT-D, the Minnesota functionals, and DLPNO-CCSD(T) converge to the same description and predict that the most likely pathways for the hydrogenation are through **TS$_D^{MI}$1(I)** and **TS$_D^{MI}$1(II)**, leading to the (S) and (R) products, respectively. Furthermore, also the path via **TS$_D^{MI}$1-(III)** is expected to contribute to the production of the (R) enantiomer.

Interestingly, although the major products are correctly identified for the pair **Sub2**− **Sub3**, most of the DFT functionals concur in predicting a larger enantiomeric excess for **Sub3** whereas the opposite is predicted by DLPNO-CCSD(T). Experimentally, when the P(o-Tol)₂-modified PHOX complex is used as catalyst, **Sub2** is found to give the larger enantiomeric excess.[8]

Finally, we note that **Sub1−3** behave in agreement with the empirical rule for trisubstituted olefins developed by Andersson,[15] since the major product is determined by the substrate complexation where the olefinic hydrogen is oriented toward the bulky substituent on the oxazoline ring, that is, complex (I) in Chart 5.

3.3.4. Sub4 and Sub5: 1,2-dihydro-7-methoxy-4-methyl-naphthalene and 1,2-dihydro-4-methyl-naphthalene. As observed in the case of **Sub3**, the phenyl moiety on the substrates **Sub4−5** can stabilize the coordination to the catalyst by stacking of the rings (coordination of type (II)) or by facing the *tert*-butyl group (coordination of type (III)), as shown in Figure 2, parts A and B, respectively. As a result, the **D1(II)** complex is calculated to be the most stable intermediate for both substrates (see SI Tables S5 and S6 for a complete overview).

Concerning the mechanism that provides the enantioselectivity, the analysis of Table 6 reveals substantial differences with respect to what was observed in the **Sub1−3** substrates. In the previous systems, the most reactive orientation was obtained when the olefinic hydrogen pointed toward the bulky substituent on the oxazoline ring to minimize steric repulsion. For **Sub4−5**, DFT methods that take into account dispersion interactions agree that the most facile pathway to obtain the (S) product is via **TS$_D^{MI}$1(III)**, as a result of the attractive interaction between the phenyl ring and the oxazoline moiety. Further complications arise from the fact that more than one path may be active in the formation of each product due to the relatively small differences in the activation energies. In the case of **Sub4**, if all four paths are considered, an e.e. = 73−89% is predicted by DFT-D, the Minnesota functionals and DLPNO-CCSD(T), in fair agreement with the experimental 72% e.e. in favor of the (S) product[60] obtained with the P(o-Tol)₂ modification of the PHOX ligand.

Andersson and co-workers[15] have investigated the asymmetric hydrogenation of **Sub5** in a combined experimental and computational study using a thiazole-based chiral ligand. Their theoretical description was able to correctly predict the major

Table 6. Asymmetric Hydrogenation of Sub4 and Sub5[a]

Sub4[b]		B3LYP	B3LYP-D	TPSSh	TPSSh-D	M06-L	M06-2X	DLPNO-CCSD(T)
(I)	(S)	**12.4**	**11.0**	**10.6**	**9.1**	**13.2**	**10.6**	**7.6**
(II)	(R)	17.1	**11.1**	15.1	**9.6**	**13.2**	**11.2**	**8.2**
(III)	(S)	15.4	**9.9**	13.1	**8.2**	**11.5**	**8.9**	**6.9**
(IV)	(R)	**12.5**	**11.9**	**10.8**	**10.2**	**12.8**	**10.7**	9.9
$\Delta\Delta G^{\ddagger}_{(R)-(S)}$		0.1	1.2	0.2	1.4	1.3	1.8	1.3
e.e.[c] (S)		3	73	18	81	74	89	83

Sub5[b]		B3LYP	B3LYP-D	TPSSh	TPSSh-D	M06-L	M06-2X	DLPNO-CCSD(T)
(I)	(S)	**11.3**	**10.1**	**9.8**	**8.5**	**12.1**	**10.1**	**7.4**
(II)	(R)	15.5	**10.5**	13.9	**9.3**	**12.2**	**10.5**	**8.0**
(III)	(S)	13.4	**8.9**	11.4	**7.3**	**10.1**	**7.9**	**6.3**
(IV)	(R)	**11.2**	**10.8**	**9.7**	**9.2**	**11.3**	**9.8**	9.7
$\Delta\Delta G^{\ddagger}_{(R)-(S)}$		−0.1	1.7	−0.1	1.9	1.2	1.9	1.8
e.e.[c] (S)			84		88	76	90	91

[a]Free energy of activation for the olefin migratory insertion as function of the relative orientation of the substrate and level of theory adopted. Energies are given in kcal/mol and are relative to the energy of the most stable **D** complex. [b]Explanation of the relative orientation of the substrate (I–IV) is given in Chart 5. For each orientation, the absolute configuration of the corresponding product is given. Bold fonts mark paths with significant activity (>1%) in the generation of the (R) and (S) products. [c]Computed using all four activation energies.

product of the reaction. However, the electronic energy separation between the major and minor product pathways was estimated to be 4.1 kcal/mol. This value is significantly larger than what the modest experimental enantiomeric excess (55%) suggests. For **Sub5**, the asymmetric hydrogenation using a catalyst close enough to the system studied here has not been reported. However, **Sub4** and **Sub5** were observed to give major products with the same absolute configuration when hydrogenated with Ir-based asymmetric catalysts;[15,62] therefore, it is reasonable to assume that the enantiomer with (S) configuration is the major product, in agreement with our theoretical prediction.

4. SUMMARY AND OUTLOOK

The catalytic cycle for the hydrogenation of ethylene and five prochiral substrates promoted by the Ir-PHOX complex was investigated by employing DFT and the recently developed DLPNO-CCSD(T) method. We determined that DFT functionals capable of treating dispersion interactions provide results that are in fair agreement with the *ab initio* data.

Concerning the mechanistic study, both the Ir^{III}/Ir^{V} and Ir^{III}/Ir^{I} families of mechanisms were considered, and we conclude that the most likely catalytic cycle involves the higher oxidation states, that is, Ir^{III}/Ir^{V}. Furthermore, the complex $[(L)Ir(H)_2(H_2)(Substrate)]^+$ is found to be the resting state of the cycle and the rate determining step of the process corresponds to the formation of the first C–H bond. This is in agreement with previous theoretical investigations.[10,15,16,23]

By investigating the formation of the first C–H bond in the case of prochiral substrates, we determined that the energy requirement for this step is minimized by the migratory insertion pathway into the metal–hydride bond. Moreover, the activation energies associated with the formation of the different enantiomers are found to be in agreement with the experimentally observed major products promoted by the catalyst.

In conclusion, we have demonstrated that one can make use of the powerful and highly systematic accuracy of coupled-cluster methods to obtain insights into organometallic reaction mechanisms and that modern implementations of correlated *ab initio* methods can be routinely used to investigate subtle chemical problems without making compromises concerning the size or complexity of the models used. Until now, such studies have been exclusively the domain of density functional methods.

ASSOCIATED CONTENT

S **Supporting Information**

Coordinates of all stationary structures, the calculated energies, as well as examples for the inputs used in the single point energy calculations. This material is available free of charge via the Internet at http://pubs.acs.org/.

AUTHOR INFORMATION

Corresponding Author
*E-mail: frank.neese@cec.mpg.de.

Notes

The authors declare no competing financial interest.

ACKNOWLEDGMENTS

REFERENCES

(1) Noyori, R. *Asymmetric Catalysis In Organic Synthesis*; Wiley: New York, 1994; pp 16–94.
(2) Knowles, W. S.; Sabacky, M. J. *Chem. Commun. (London)* **1968**, 1445–1446.
(3) Ikariya, T.; Ishii, Y.; Kawano, H.; Arai, T.; Saburi, M.; Yoshikawa, S.; Akutagawa, S. *J. Chem. Soc., Chem. Commun.* **1985**, 922–924.
(4) Tang, W.; Zhang, X. *Chem. Rev.* **2003**, *103*, 3029–3070.
(5) Crabtree, R. *Acc. Chem. Res.* **1979**, *12*, 331–337.
(6) Lightfoot, A.; Schnider, P.; Pfaltz, A. *Angew. Chem., Int. Ed.* **1998**, *37*, 2897–2899.
(7) Helmchen, G.; Pfaltz, A. *Acc. Chem. Res.* **2000**, *33*, 336–345.
(8) Pfaltz, A.; Blankenstein, J.; Hilgraf, R.; Hörmann, E.; McIntyre, S.; Menges, F.; Schönleber, M.; Smidt, S. P.; Wüstenberg, B.; Zimmermann, N. *Adv. Synth. Catal.* **2003**, *345*, 33–43.
(9) Woodmansee, D. H.; Pfaltz, A. In *Iridium Catalysis*; Andersson, P. G., Ed.; Springer-Verlag: Berlin, 2011; Vol. *34*, pp 31–76.
(10) Brandt, P.; Hedberg, C.; Andersson, P. G. *Chem.—Eur. J.* **2003**, *9*, 339–347.
(11) Fan, Y.; Cui, X.; Burgess, K.; Hall, M. B. *J. Am. Chem. Soc.* **2004**, *126*, 16688–16189.

(12) Cui, X.; Fan, Y.; Hall, M. B.; Burgess, K. *Chem.—Eur. J.* **2005**, *11*, 6859−6868.

(13) Gridnev, I. D.; Imamoto, T. *Acc. Chem. Res.* **2004**, *37*, 633−644.

(14) Dietiker, R.; Chen, P. *Angew. Chem., Int. Ed.* **2004**, *43*, 5513−5516.

(15) Church, T. L.; Rasmussen, T.; Andersson, P. G. *Organometallics* **2010**, *29*, 6769−6781.

(16) Hopmann, K. H.; Bayer, A. *Organometallics* **2011**, *30*, 2483−2497.

(17) Dirac, P. *Proc. R. Soc. (London) A* **1929**, *123*, 714−733.

(18) Slater, J. C. *Phys. Rev.* **1951**, *81*, 385−390.

(19) Becke, A. D. *Phys. Rev. A* **1988**, *38*, 3098−3100.

(20) Lee, C.; Yang, W.; Parr, R. G. *Phys. Rev. B* **1988**, *37*, 785−789.

(21) Becke, A. D. *J. Chem. Phys.* **1993**, *98*, 5648−5652.

(22) Grimme, S.; Antony, J.; Ehrlich, S.; Krieg, H. *J. Chem. Phys.* **2010**, *132*, 154104−19.

(23) Mazuela, J.; Norrby, P.-O.; Andersson, P. G.; Pàmies, O.; Diéguez, M. *J. Am. Chem. Soc.* **2011**, *133*, 13634−13645.

(24) Harvey, J. N. *Annu. Rep. Prog. Chem., Sect. C: Phys. Chem.* **2006**, *102*, 203−226.

(25) Cohen, A. J.; Mori-Sanchez, P.; Yang, W. *Science* **2008**, *321*, 792−794.

(26) Bartlett, R. J.; Musiał, M. *Rev. Mod. Phys.* **2007**, *79*, 291−352.

(27) Saebø, S.; Pulay, P. *J. Chem. Phys.* **1987**, *86*, 914−922.

(28) Saebø, S.; Pulay, P. *J. Chem. Phys.* **1988**, *88*, 1884−1890.

(29) Hampel, C.; Werner, H.-J. *J. Chem. Phys.* **1996**, *104*, 6286−6297.

(30) Schütz, M.; Werner, H.-J. *J. Chem. Phys.* **2001**, *114*, 661−681.

(31) Subotnik, J. E.; Sodt, A.; Head-Gordon, M. *J. Chem. Phys.* **2006**, *125*, 074116−12.

(32) Riplinger, C.; Neese, F. *J. Chem. Phys.* **2013**, *138*, 034106−18.

(33) Riplinger, C.; Sandhoefer, B.; Hansen, A.; Neese, F. *J. Chem. Phys.* **2013**, *139*, 134101−13.

(34) Neese, F.; Hansen, A.; Liakos, D. G. *J. Chem. Phys.* **2009**, *131*, 064103−15.

(35) Neese, F.; Wennmohs, F.; Hansen, A. *J. Chem. Phys.* **2009**, *130*, 114108−18.

(36) Anoop, A.; Thiel, W.; Neese, F. *J. Chem. Theory Comput.* **2010**, *6*, 3137−3144.

(37) Liakos, D. G.; Hansen, A.; Neese, F. *J. Chem. Theory Comput.* **2011**, *7*, 76−87.

(38) Eichkorn, K.; Treutler, O.; Öhm, H.; Häser, M.; Ahlrichs, R. *Chem. Phys. Lett.* **1995**, *240*, 283−290.

(39) van Wüllen, C. *J. Chem. Phys.* **1998**, *109*, 392−399.

(40) Schäfer, A.; Horn, H.; Ahlrichs, R. *J. Chem. Phys.* **1992**, *97*, 2571−2577.

(41) Weigend, F.; Ahlrichs, R. *Phys. Chem. Chem. Phys.* **2005**, *7*, 3297−3305.

(42) Weigend, F. *Phys. Chem. Chem. Phys.* **2006**, *8*, 1057−1065.

(43) Pantazis, D. A.; Chen, X.-Y.; Landis, C. R.; Neese, F. *J. Chem. Theory Comput.* **2008**, *4*, 908−919.

(44) Klamt, A.; Schüürmann, G. *J. Chem. Soc., Perkin Trans. 2* **1993**, 799−805.

(45) Cramer, C. J. *Essentials of Computational Chemistry: Theories and Models*, 2nd ed.; John Wiley & Sons: New York, 2005; pp 355−384.

(46) Grimme, S. *Chem.—Eur. J.* **2012**, *18*, 9955−9964.

(47) Perdew, J. P.; Wang, Y. *Phys. Rev. B* **1992**, *45*, 13244−13249.

(48) Staroverov, V. N.; Scuseria, G. E.; Tao, J.; Perdew, J. P. *J. Chem. Phys.* **2003**, *119*, 12129−12137.

(49) Tao, J.; Perdew, J. P.; Staroverov, V. N.; Scuseria, G. E. *Phys. Rev. Lett.* **2003**, *91*, 146401−4.

(50) Zhao, Y.; Truhlar, D. G. *Acc. Chem. Res.* **2008**, *41*, 157−167.

(51) Zhao, Y.; Truhlar, D. G. *Theor. Chem. Acc.* **2008**, *120*, 215−241.

(52) Neese, F.; Wennmohs, F.; Hansen, A.; Becker, U. *Chem. Phys.* **2009**, *356*, 98−109.

(53) Kossmann, S.; Neese, F. *Chem. Phys. Lett.* **2009**, *481*, 240−243.

(54) Neese, F. *WIREs Comput. Mol. Sci.* **2012**, *2*, 73−78.

(55) Mazet, C.; Smidt, S. P.; Meuwly, M.; Pfaltz, A. *J. Am. Chem. Soc.* **2004**, *126*, 14176−14181.

(56) Each stable type of intermediate is identified with a capital letter **A−I**; Transition states are labeled TS_X^Y where X is the stable intermediate preceding the TS, and Y distinguishes (when necessary) the mechanisms: Migratory Insertion vs Metathesis. The number **1−4** identifies the specific isomers, for example, 1 and 3, the substrate is *trans* to P, and 2 and 4, substrate *trans* to N. Lower case **p** indicates that the double bond lies on the plan defined by the N−Ir−P.

(57) Smidt, S. P.; Zimmermann, N.; Studer, M.; Pfaltz, A. *Chem.—Eur. J.* **2004**, *10*, 4685−4693.

(58) Kozuch, S.; Shaik, S. *Acc. Chem. Res.* **2011**, *44*, 101−110.

(59) Seeman, J. I. *Chem. Rev.* **1983**, *83*, 83−134.

(60) Smidt, S. P.; Menges, F.; Pfaltz, A. *Org. Lett.* **2004**, *6*, 2023−2026.

(61) Blackmond, D. G.; Lightfoot, A.; Pfaltz, A.; Rosner, T.; Schnider, P.; Zimmermann, N. *Chirality* **2000**, *12*, 442−449.

(62) Trifonova, A.; Diesen, J. S.; Andersson, P. G. *Chem.—Eur. J.* **2006**, *12*, 2318−2328.